

We are IntechOpen, the world's leading publisher of Open Access books Built by scientists, for scientists

6,900

Open access books available

186,000

International authors and editors

200M

Downloads

Our authors are among the

154

Countries delivered to

TOP 1%

most cited scientists

12.2%

Contributors from top 500 universities



WEB OF SCIENCE™

Selection of our books indexed in the Book Citation Index
in Web of Science™ Core Collection (BKCI)

Interested in publishing with us?
Contact book.department@intechopen.com

Numbers displayed above are based on latest data collected.
For more information visit www.intechopen.com



Investigation and Analysis of the Mechanical Behaviors of the Electric Vehicles

Liang Zheng

Additional information is available at the end of the chapter

<http://dx.doi.org/10.5772/53275>

1. Introduction

An electric vehicle (EV), also referred to as an electric drive vehicle, uses one or more electric motors or traction motors for propulsion. Electric vehicles are being widely developed due to their better performance than the traditional fuel vehicles in terms of environmental pollution and energy consumption [1-3]. However, comparing with the traditional petroleum vehicles, the relatively short driving distance of the electric vehicle is the main hindrance to prevail. To improve the performance of the electric vehicle and excel the internal combustion engine vehicles, research and study need to be done. In this chapter, analyses and applications are developed to investigate the mechanical behaviors of the electric vehicles such that the performance of the electric vehicles can be considerably improved.

2. Investigation of the regenerative braking force in electric vehicles

In order to overcome the weakness of the short driving distance, the energy efficiency of the electric vehicle has to be substantially improved [4]. The regenerative braking technology is able to convert the excessive kinetic energy of the vehicle into another form, which can be either used immediately or stored until needed [5]. In this section, the regenerative braking force is analyzed and an optimized control strategy for the regenerative braking process was proposed based on the results of the analysis. With the implementation of this optimized control strategy, the energy efficiency of the electric vehicle can be appreciably improved.

2.1. Analysis of the regenerative braking force

The amount of recovered energy during the braking process depends on the magnitude of the regenerative braking force. In order to achieve the maximum amount of recovered energy, the forces in the front and rear tires of the vehicle during the braking process should be analyzed and distributed at the optimal level. Figure 1 represents a schematic of the vehicle during the braking process in which the deceleration of the vehicle is denoted as j , the gravitational acceleration is denoted by g and the braking forces in the front and the rear wheels are denoted as F_{xb1} and F_{xb2} , respectively.

Force Equilibrium yields:

$$F_{z1} = mg\left(\frac{b}{L} + \frac{j}{g} \frac{h_g}{L}\right) \text{ and } F_{z2} = mg\left(\frac{a}{L} - \frac{j}{g} \frac{h_g}{L}\right) \tag{1}$$

The braking rate z and the adhesion coefficient Φ_i are defined as:

$$z = \frac{j}{g} \text{ and } \Phi_i = \frac{F_{xbi}}{F_{zi}} \tag{2}$$

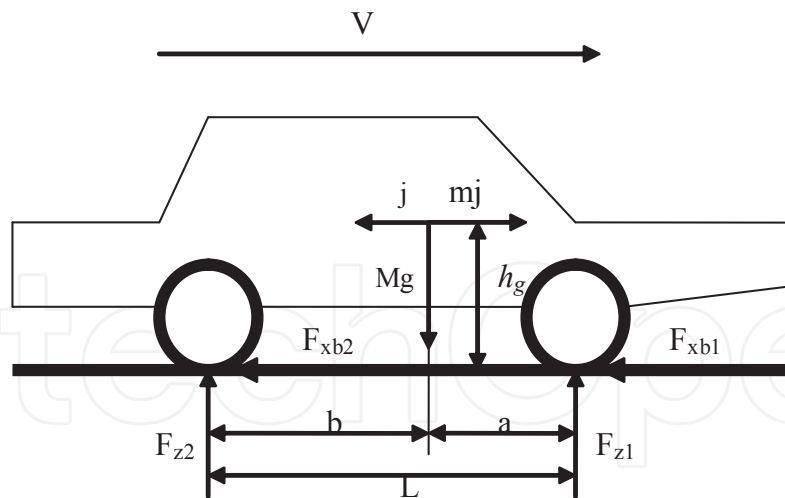


Figure 1. Schematic of the vehicle during the braking process.

In general, there are three different scenarios due to the various distribution of the braking forces in the front and rear wheels: i) both the front and rear wheels are locked at the same time; ii) the front wheels are locked whereas the rear wheels are unlocked; and iii) the rear wheels are locked whereas the front wheels are unlocked.

The first scenario is the ideal case that has the best braking effect. The relationship between the forces in the front and rear wheels can be derived and expressed as:

$$F_{xb2} = \frac{1}{2} \left[\frac{mg}{h_g} \sqrt{b^2 + \frac{4h_g L}{mg} F_{xb1}} - \left(\frac{mgb}{h_g} + 2F_{xb1} \right) \right] \quad (3)$$

The second scenario is a dangerous case in which the vehicle loses the steering capability but it won't be rolled over. The relationship between the forces in the front and rear wheels in this scenario can be shown as:

$$F_{xb2} = F_{xb1} \left(\frac{L - \Phi h_g}{\Phi h_g} \right) - \frac{mgb}{h_g} \quad (4)$$

The third scenario is an extremely dangerous case in which a rollover may be occurred. The relationship between the forces in the front and rear wheels in this case can be derived and written as:

$$F_{xb2} = \frac{\Phi}{L + \Phi h_g} (mga - h_g F_{xb1}) \quad (5)$$

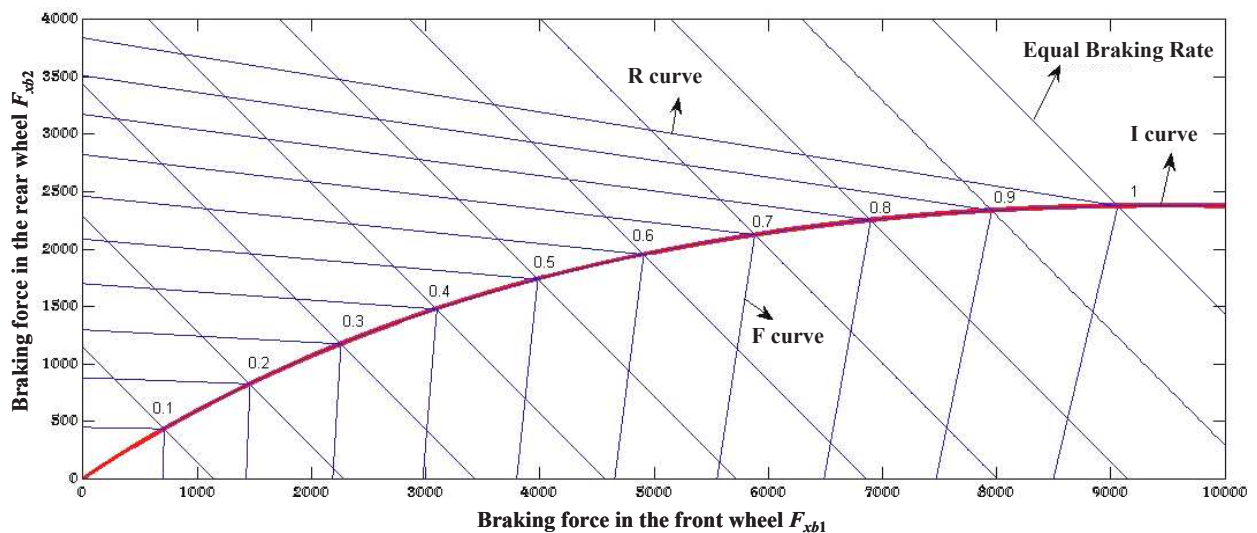


Figure 2. Plots represent the relationships between the braking forces in the front and rear wheels.

Based on Eqs. (3)~(5), the relationships between forces in the front and rear wheels of the electric vehicle in these three different scenarios can be plotted and shown in Fig.2. I curve, as illustrated with red dark color, represents the first scenario (i.e., the ideal case); the sec-

ond scenario is represented by a series of F curves; and R curves represent the third scenario which is the extremely dangerous case.

The above analysis reveals that the distribution of the braking forces between the front and rear wheels plays the crucial role on the braking performance of the vehicle. In order to ensure the braking safety of the vehicle, United Nations Economic Commission for Europe (UNECE) established a regulation (ECE R13) which strictly regulates the distribution range of the braking forces between the front and rear wheels, as shown in Fig. 3 [6]. The horizontal axis z represents the braking ratio, and the vertical axis k is the adhesion coefficient between the tire and the road in the figure.

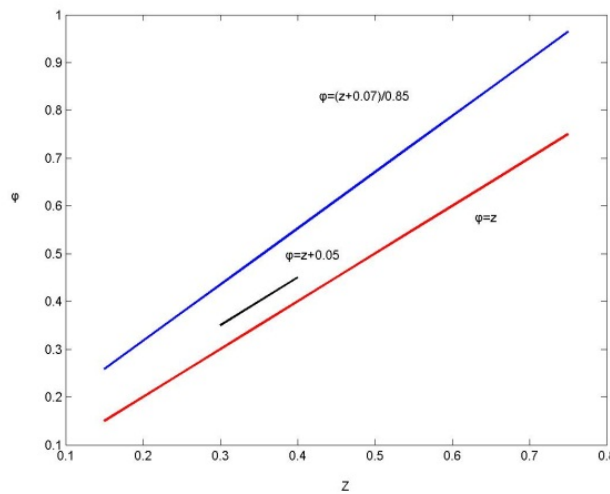


Figure 3. Diagram representing the braking requirements stated in ECE R13 [6].

According to ECE R13, the adhesion coefficient needs to satisfy $k < (z+0.07)/0.85$, which results in:

$$F_{xb1} + F_{xb2} = mgz \quad \text{and} \quad F_{xb1} = \frac{z + 0.07}{0.85} \cdot \frac{mg}{L} (b + zh_g) \tag{6}$$

The braking ratio z can be vanished and it yields:

$$\frac{(F_{xb1} + F_{xb2})^2}{mgL} + \frac{F_{xb1} + F_{xb2}}{L} (b + 0.07h_g) + \frac{0.07mgb}{L} - 0.085F_{xb1} = 0 \tag{7}$$

In addition, the adhesion coefficient of the rear wheel has to be less than that of the front wheel to avoid the occurrence of the extremely dangerous scenario. This means:

$$k_2 = \frac{F_{xb2}}{F_{z2}} \leq k_1 = \frac{F_{xb1}}{F_{z1}} \Rightarrow \frac{F_{xb1}}{F_{xb2}} \geq \frac{b + h_g z}{a - h_g z} \text{ and } F_{xb1} + F_{xb2} = mgz \quad (8)$$

The braking ratio z can be cancelled and it becomes:

$$F_{xb2} = \frac{1}{2} \left[\frac{mg}{h_g} \sqrt{b^2 + \frac{4h_g L}{mg} F_{xb1}} - \left(\frac{mgb}{h_g} + 2F_{xb1} \right) \right] \quad (9)$$

which evidently matches with the ideal distribution I curve.

Using Eqs. (7) and (9), the distribution range of the braking forces in front and rear wheels can be plotted and shown in Fig. 4. It can be seen from Fig. 4 that I curve represents Eq. (9) and M curve represents Eq. (9). The acceptable braking forces in the front and rear wheels should be distributed between the range enclosed by I curve and M curve, according to the technical requirements stated in ECE R13.

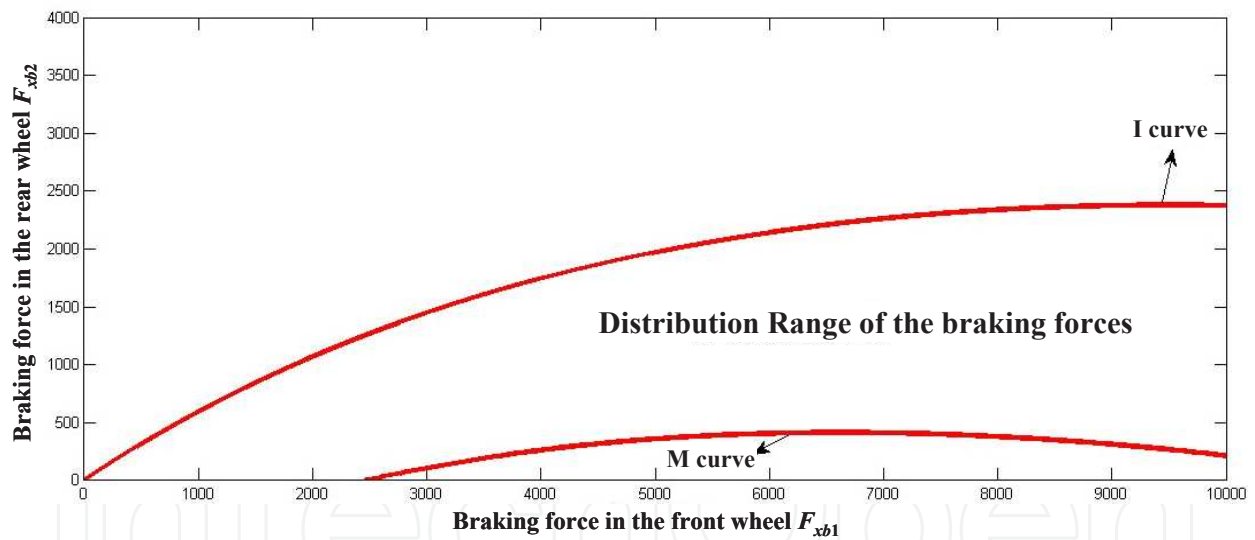


Figure 4. The distribution range of the braking forces in front and rear wheels, satisfying ECE R13.

2.2. An optimized control strategy of the regenerative braking

Based on the analysis developed in the previous section, an optimized control strategy of the regenerative braking process is proposed in this section. This proposed control strategy aims at the following three goals: 1) safety of the vehicle braking; 2) maximization of the recovered energy; 3) a simple control system with a low cost of manufacturing. A front-wheel drive pure electric vehicle is utilized in this research, with the parameters listed in Table 1.

Pure Electric Vehicle	Mass	1144 kg
	Drag coefficient	0.335
	Height of center of mass	0.5m
	Frontal area	2.0 m ²
	Wheelbase	2.6 m
	Coefficient of rolling resistance	0.009
	Distance between center of mass and front axle	1.04 m
AC Induction Motor	Nominal power	75 KW
	Nominal rotating speed	2640 r/min
	Maximum rotating speed	10000 r/min
	Maximum torque	271 N·M
	Overload factor	1.8
Gear	Gear reduction ratio	6.6732
	Main gear reduction ratio	1
Power	Lead acid battery pack	

Table 1. Parameters of the pure electric vehicle utilized in this research.

The energy due to the regenerative braking can be recovered when the braking rate is between 0 and 0.6. No energy will be recovered when the braking rate is higher than 0.6. The optimal distribution of the braking forces between the front and rear wheels is presented as the OGFC-I curve shown in Fig. 5.

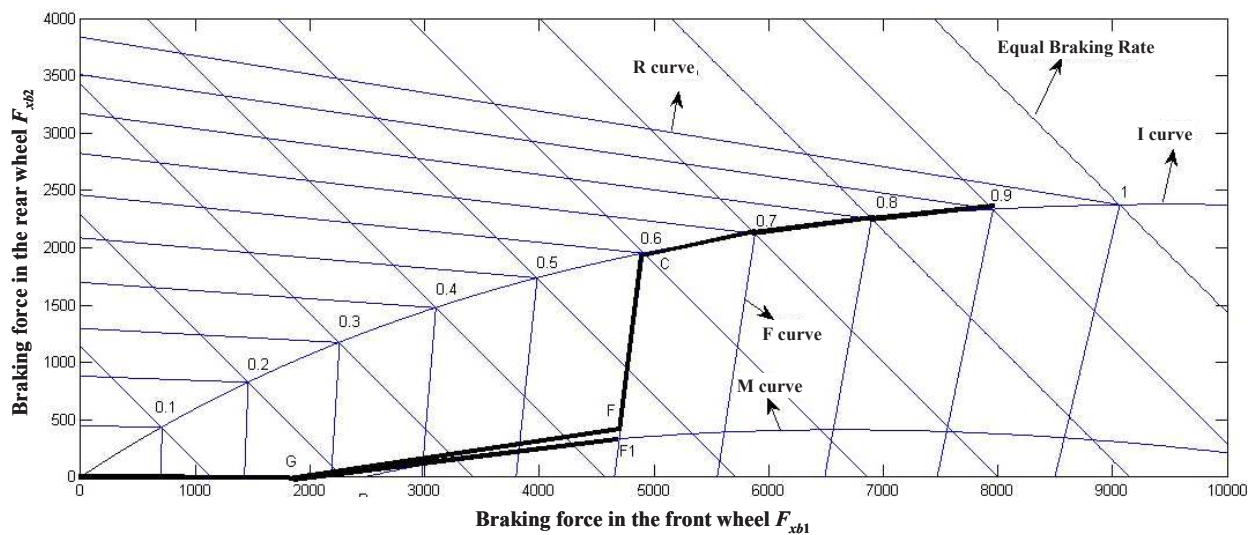


Figure 5. Optimized distribution curve of braking forces in front and rear wheels.

1. $0 < z \leq 0.16$

The braking forces in the front and rear wheels are distributed along the line segment OG.

2. $0.16 < z \leq 0.455$

The braking forces in the front and rear wheels are distributed along the line segment GF. The line GF₁ is tangent to M curve and the equation for GF₁ can be expressed as:

$$F_{xb2} = 0.12F_{xb1} - 219.6 \quad (10)$$

In order to keep distant from the M curve that the rear wheel may be locked before the front wheel which can result in a rollover, one can chose the line segment GF instead of GF₁. The line GF can be presented by:

$$F_{xb2} = 0.15F_{xb1} - 219.6 \quad (11)$$

3. $0.455 < Z \leq 0.6$

The braking forces in the front and rear wheels are distributed along the line segment FC. With the increase of the braking rate, it quickly approaches to I curve. The line segment FC can be described as:

$$F_{xb2} = \frac{23}{3}F_{xb1} - 35692.8 \quad (12)$$

4. $Z > 0.6$

It is the case of emergency braking, the braking forces in the front and rear wheels are distributed along the ideal case (as described in I curve).

2.3. Modeling and simulations

Implementing the optimized control strategy in Section III, the controlling module of the braking force was established and plugged into the commercial software ADVISOR. The distribution modules of the optimized braking forces in the front and rear wheels are shown in Fig. 6.

In order to validate this optimized controlling strategy, three drive cycles were used, i.e., CYC_ARTERIAL, CYC_LA92, and CYC_NYCC. The parameters of these three drive cycles are listed in Table 2.

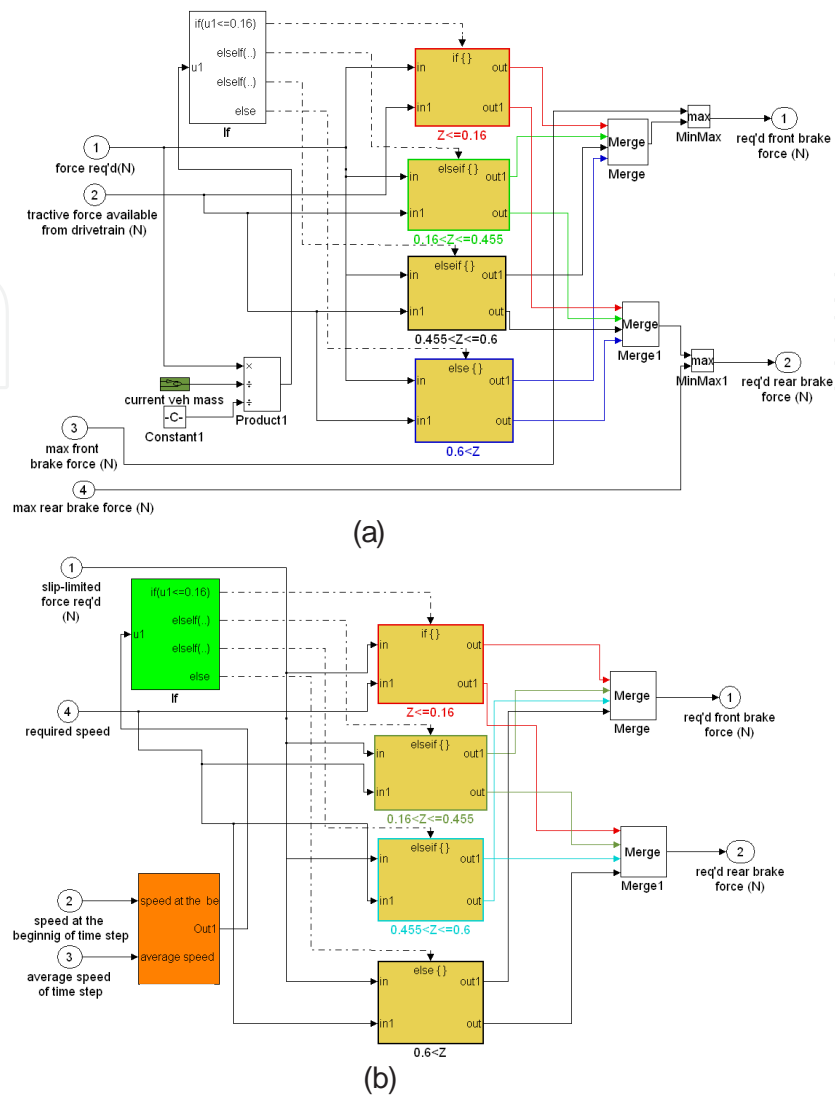


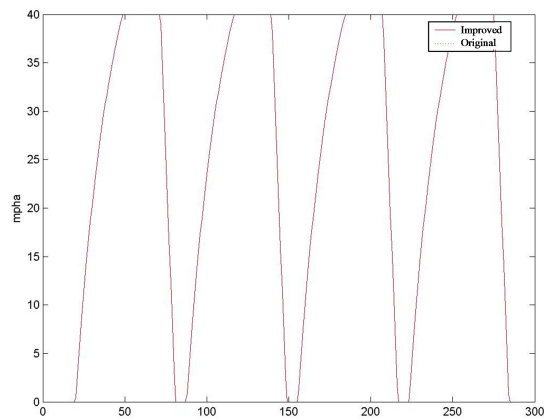
Figure 6. Distribution Modules of the optimized braking forces in the (a) front and (b) rear wheels.

The pure electric vehicle was simulated in these three drive cycles in ADVISOR, using the optimized control strategy. Then the obtained results were compared with the actual (original) results. Figure 7 represents the comparisons of the two sets of results in CYC_ARTERIAL and CYC_NYCC drive cycles. It can be seen from Fig. 7 that these two sets of results match very well, meaning that the optimized control strategy did not affect the safety of the vehicle.

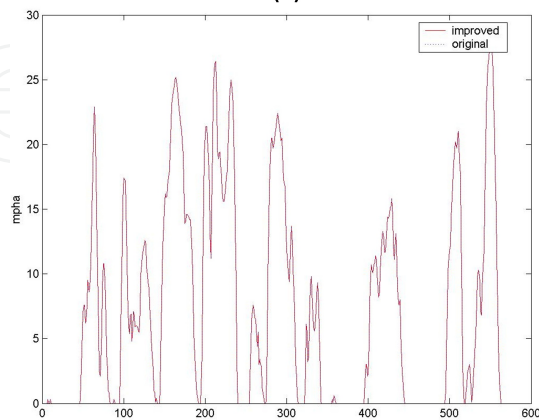
The ADVISOR software has a default control strategy which is easy to operate but can not recycle much energy due to the regenerative braking. More importantly, the default control strategy is unable to guarantee a quick and safe stop for the high-speed running vehicle due to the limited amount of regenerative braking force generated during the braking process. Here, the results using the optimized control strategy are compared to the results using the default control strategy provided by ADVISOR.

Parameters	CYC_ARTERIAL	CYC_LA92	CYC_NYCC
Time (s)	291	1435	598
Max. speed (km/h)	64.3	108.1	44.58
Avg. speed (km/h)	39.7	39.6	21.4
Max. acceleration (m/s ²)	1.07	3.08	2.68
Max. deceleration (m/s ²)	-2.01	-3.93	-2.64
Avg. acceleration (m/s ²)	0.6	0.67	0.62
Avg. deceleration (m/s ²)	-1.8	-0.75	-0.61
Stops	4	16	18
Driving distance (km)	3.2	15.8	1.9

Table 2. Parameters of three drive cycles



(a)



(b)

Figure 7. Comparisons of the vehicle speed in (a) CYC_ARTERIAL and (b) CYC_NYCC cycles.

Firstly, the SOC of the battery is selected to be compared by using these two different control strategies. Figure 8 illustrates the comparisons of SOC in CYC_LA92 and CYC_NYCC drive cycles, using the default and optimized control strategies. It can be seen that the SOC curve using the optimized control strategy has a flatter slope than the SOC curve using the default one. It means more electric energy is reserved in the battery and consequently more kinetic energy can be recovered during the regenerative braking process.

Secondly, the recovered energy during the braking process will be compared using these two different control strategies. As listed in Tables 3 to 5, the parameters for comparison include the consumed energy, the braking energy, the total recovered energy, the energy recovery efficiency, the effective energy recovery efficiency, and the energy efficiency of the entire vehicle. The optimized control strategy and the default control strategy in ADVISOR are employed in the three drive cycles.

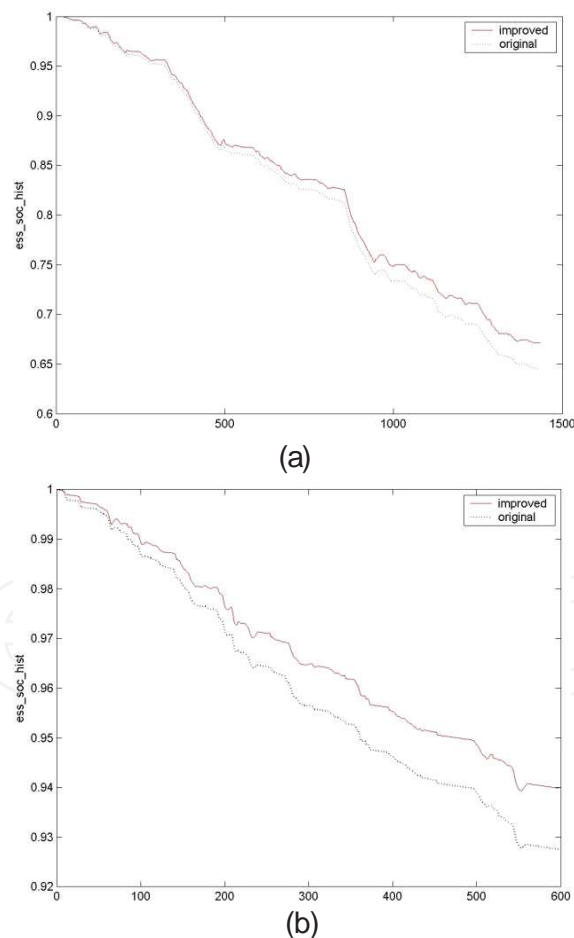


Figure 8. Comparisons of SOC in (a) CYC_LA92 and (b) CYC_NYCC cycles, using two different control strategies.

Parameters	Optimized Control Strategy	Default Control Strategy
Total Energy Consumption (KJ)	2198	2172
Braking Energy (KJ)	671	671
Recovered Energy (KJ)	409	299
Energy Recovery Efficiency	60.95%	44.56%
Effective Energy Recovery Efficiency	18.6%	13.77%
Energy Efficiency of the entire vehicle	36.5%	34.8%

Table 3. Comparison of the recovered energy in the CYC_ARTERIAL cycle

Parameters	Optimized Control Strategy	Default Control Strategy
Total Energy Consumption (KJ)	11168	11209
Braking Energy (KJ)	2891	2891
Recovered Energy (KJ)	1740	1066
Energy Recovery Efficiency	60.2%	36.87%
Effective Energy Recovery Efficiency	15.6%	9.5%
Energy Efficiency of the entire vehicle	42.6%	39.6%

Table 4. Comparison of the recovered energy in the CYC_LA92 drive cycle

Parameters	Optimized Control Strategy	Default Control Strategy
Total Energy Consumption (KJ)	2040	2212
Braking Energy (KJ)	565	565
Recovered Energy (KJ)	277	116
Energy Recovery Efficiency	49.02%	20.53%
Effective Energy Recovery Efficiency	13.6%	5.2%
Energy Efficiency of the entire vehicle	13.5%	11.3%

Table 5. Comparison of the recovered energy in the CYC_NYCC drive cycle

It can be seen from Tables 3 to 5 that with the use of the optimized control strategy, the parameters of all categories have been improved considerably, comparing with the acquired results using the default control strategy. With the same amount of braking energy, the energy recovered from the regenerative braking process has been increased dramatically via the use of the optimized control strategy, for all three drive cycles. For instance, in the CYC_NYCC drive cycle, the amount of recovered energy using the optimized control strategy (i.e., 277 KJ) is more than doubled, comparing to the number (116 KJ) utilizing the default control strategy provided by ADVISOR. In addition, the energy efficiency of the entire vehicle has also been improved for all three drive cycles, via the use of the optimized control strategy. The largest improvement occurs in the CYC_NYCC drive cycle with the amount of almost 20% (13.5% vs. 11.3%), with less total energy consumption (2040 KJ vs. 2212 KJ). The optimized control strategy also prevails over the default control strategy in other categories, as shown in Tables 3 to 5.

2.4. Summary on the analysis of the regenerative braking Force

In this section, the regenerative braking force was analyzed and the distribution range of the braking forces in the front and rear wheels was determined to meet the requirements in UNECE R13. An optimized control strategy of the regenerative braking process was proposed based on the results of the analysis. The regenerative braking process with the optimized control strategy is simulated in the commercial software ADVISOR. Three different drive cycles with real data and the default control strategy in ADVISOR were employed to conduct the comparison. Results of the comparison reveal that the optimized control strategy prevails over the default control strategy in every category of energy recovery. Comparing to the default control strategy, this optimized control strategy can improve the energy recovery efficiency by more than 100% for one drive cycle. This optimized control strategy can also be used for the hybrid vehicles.

3. Simulation and analysis of Series Hybrid Electric Vehicle (SHEV)

Series-hybrid vehicles are driven by the electric motor with no mechanical connection to the engine. Unlike piston internal combustion engines, electric motors are efficient with exceptionally high power-to-weight ratios providing adequate torque over a wide speed range. In a series-hybrid system, the combustion engine drives an electric generator instead of directly driving the wheels. The generator provides power for the driving electric motors [7]. However, the efficiency of the engine and the working condition of the battery have to be considerably improved to make the series hybrid electric vehicles more competitive in the industry. In order to improve the efficiency of the engine and make the battery work in the better condition, analyses and simulations need to be developed and an optimized control strategy has to be obtained and utilized.

3.1. Control strategy for SHEVs

3.1.1. Operation mode for SHEVs

A typical power control flow for SHEVs can be described by the following four kinds of operation modes, as shown in Fig. 9 [8].

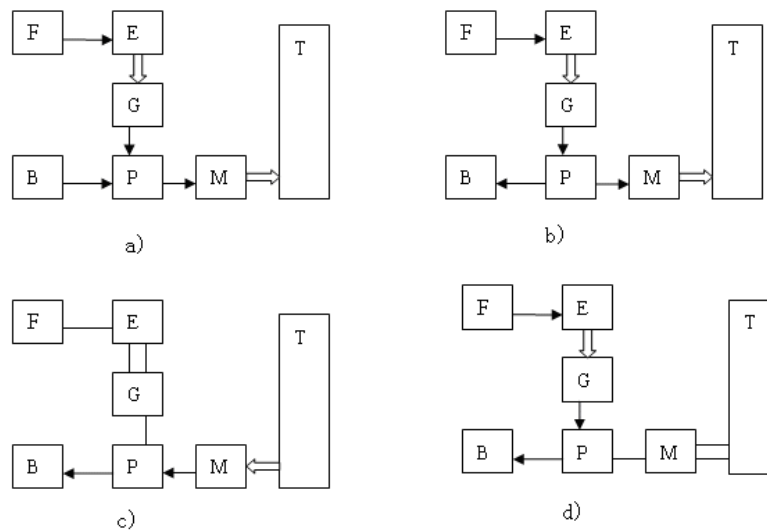


Figure 9. A typical power control flow for SHEVs.

When a SHEV starts to run, the engine outputs the electrical energy via the generator and the battery, transmits the energy to the converter, which drives the motors, ultimately drive wheels through the mechanical transmission devices; When the vehicle is underloaded, the power outputted by the engine is more than the vehicle needs, then the excessive energy is utilized to recharge the battery via the generator, until the SOC reaches the predetermined limit; When the vehicle is braking or decelerating, the motor converts the kinetic energy into the electrical energy, recharging the battery through the power converter; When the vehicle stops, the engine can recharge the battery through generators and power converters.

3.1.2. Control strategy for SHEVs

During the SHEV automobile working process, it often happens that energies from two or more sources superimpose. The main purpose of the correct matching of SHEV powertrain is to rationally determine the operating characteristics of the engine and its power distribution and energy balance with the energy storage device. By controlling the working status of various energy sources, the energy conversion efficiency can be improved, the loss due to energy transmission can be reduced, and ultimately the energy can be utilized in a maximum way for SHEVs.

The general control strategy for SHEVs is developed normally based on the parameters such as battery SOC, the driver's accelerator pedal position, the wheel speed and the average

power of the driving wheel; then the engine and electric motor generate the corresponding torque to meet the requirements of the driving torque for the driving wheel. Commonly used control strategies include "thermostat" and "power follower" [9], where the power follower strategy are described as follows:

1. When the battery SOC is greater than the upper limit of SOC_{max} , the engine stops working, but when the power demand of vehicle is too large, the engine needs to be restarted;
2. When the battery SOC is less than the lower limit SOC_{min} , the engine needs to get to work;
3. When the engine works, its power output should not only follow the changes of the power demand of the vehicle, but keep the battery SOC around the middle value of its working range;
4. While the engine is working, its output power should not be too small or too large in order to ensure high efficiency.

In this research, parameters are controlled to determine the energy flow of SHEVs, so that the control strategy of "power follower + thermostat" is designed. The general logic control flow is shown in Fig. 10.

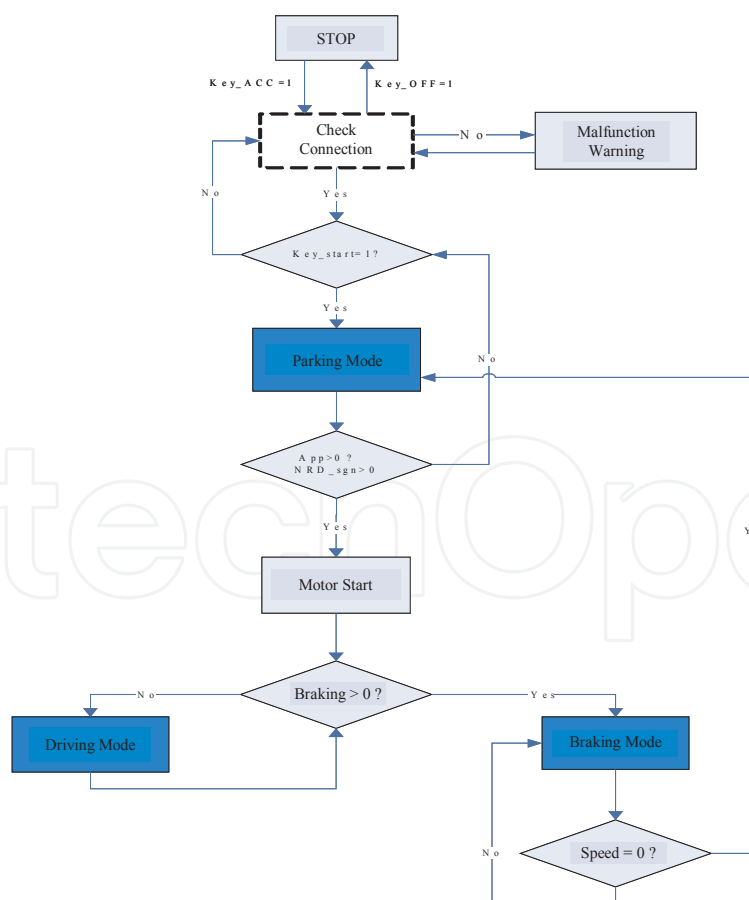


Figure 10. General logic control.

3.1.3. SIMULINK/stateflow control process

Based on the above analysis, one can establish the vehicle control systems in the SIMULINK/Stateflow based on the energy flow of vehicles. Modeling in the SIMULINK/Stateflow, one can not only avoid the complex programming in MATLAB, but omit the direct construction of control frame in the SIMULINK. Furthermore, the status flow in Stateflow can explicitly represent the control process with figures, so that the control can be precisely achieved. Based on the above analysis and the energy flow analysis and control chart, the control flow designed in the SIMULINK/Stateflow is shown in Fig. 11.

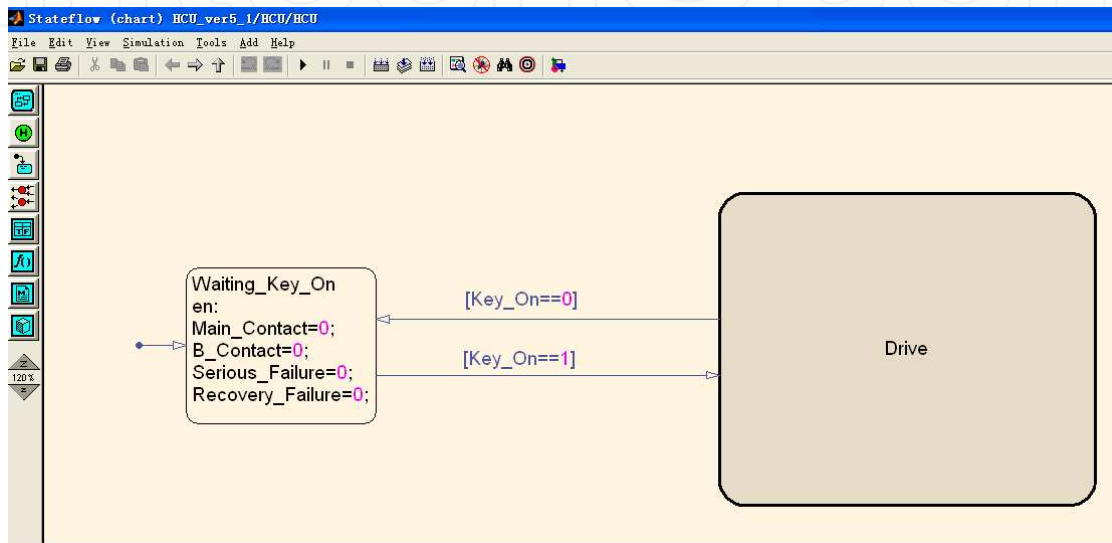


Figure 11. Stateflow control process.

The kernel part of this design is the driving component, which is shown Fig. 12.

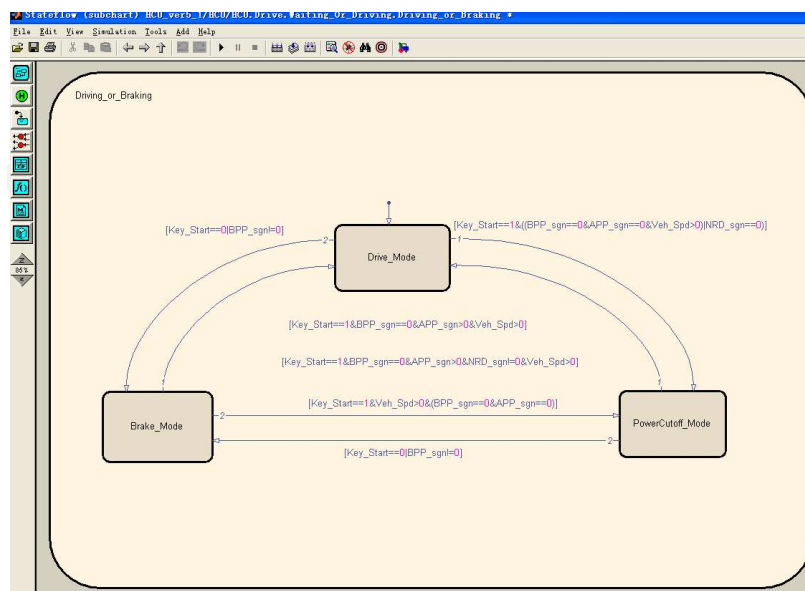


Figure 12. Status Flow of the Driving Component.

3.2. Simulations of SHEVs

ADVISOR employs a unique hybrid simulation method, which mixes the backward simulation and the forward simulation, with the backward simulation as the primary one and forward simulation as the auxiliary one [10]. It first carries on the backward simulation along with the opposite direction to the actual power flow, making the request of the needed speed and torque to the vehicle model according to requirement of the path circulation. Then the vehicle model delivers the request to the wheel and the axle module, to the main gearbox module, to the transmission gearbox module and so on, until the request is delivered to the power supply module, then the power provided by the power supply can be calculated. Next, it carries on the forward simulation; a stepwise computation will be developed along the actual direction of the power flow, until the automobile's real speed is determined.

3.2.1. Power matching of various parts of vehicles

3.2.1.1. Power selection for engines

SHEVs have the similar requirements to ordinary vehicles on dynamic performance, and continuous driving distance has to be independent of battery capacity, thus the engine's maximum output power needs to satisfy [11]:

$$P_{e_{\max}} = \frac{1}{3600\eta_{gc}\eta_{mc}} \left(mgf + \frac{C_D A v_{a_{\max}}^2}{21.55} \right) v_{a_{\max}} \quad (13)$$

where $P_{e_{\max}}$ is the maximum output power of the engine; η_{gc} is the power conversion efficiency; η_{mc} is motor efficiency; $v_{a_{\max}}$ is average driving speed; m is the vehicle mass; g is the acceleration due to gravity; f is the rolling resistance coefficient; C_D is the air resistance coefficient; A is the windward area.

Table 6 lists the parameters for the SHEV engine.

Maximum Rotating Speed	Normal Rated Power / Rotating Speed	Maximum Torque / Rotating Speed
4200 rpm	96 kw / 4200 rpm	300 N-m / 3000 rpm

Table 6. SHEV Engine Parameters

3.2.1.2. Selection of parameters for motors

Parameters of the motor should be chosen to meet the requirements of a wide range of vehicle speed and load variation. The to-be-determined parameters mainly include the low-speed constant power P_{mr} , rated speed of motor n_{mr} , max. speed of motor $v_{m_{\max}}$ and rated voltage of motor V_{mr} .

Rated speed and maximum speed of motor: the maximum speed has an impact on the size of the transmission system and rated torque of motor, where the rated speed of the motor can be expressed as:

$$n_{mr} = n_{m\max} / \beta \quad (14)$$

where β is the ratio between the maximum speed and rated speed of the motor, also known as the coefficient of expanded constant power zone of the motor. Usually this coefficient is chosen from 4 ~ 6.

Rated power, maximum power of Motor: for SHEVs, the selection of power parameters for the motor must meet the performance requirements. In a road with good condition, the vehicle's power balance equation can be written as follows [12]:

$$T = \frac{1}{3.6} \int_0^v \frac{dt}{dv} dv = \frac{1}{3.6} \int_0^v \frac{\delta m}{F_t - F_w - F_f} dv \quad (15)$$

where T is the time for the speed accelerated from 0 to v ; δ is the spinning mass conversion factor; F is the driving force; F_w is the air resistance; and F_f is rolling resistance.

The climbing capacity of a vehicle can be represented by the angle of the slope that the vehicle can climb under a certain speed, which is described as [13]:

$$\alpha = \arcsin\left(\frac{F_t - F_w}{mg\sqrt{1 + f^2}}\right) - \arctan(f) \quad (16)$$

where, α is the slope angle; mg is weight of the vehicle, and f is rolling resistance coefficient.

According to the situation with acceleration and the situation with the highest speed, the needed power can be calculated for the running vehicle. Next, according to the maximum calculated value, considering the transmission efficiency, the power for the electric motor can be preliminarily determined. Then this value can be substituted back to the above two equations for verification. Once the maximum power of the motor is determined, the rated power of the electric motor can be calculated according to the equation below:

$$P_{on} = \frac{P_{m\max}}{\lambda} \quad (17)$$

in which, P_{on} is the rated power of the electric motor; $P_{m\max}$ is the maximum power of the electric motor; λ is overload factor of the electric motor.

Table 7 lists the parameters of the motor for SHEVs.

Peak Torque	Peak Power	Rated Power	Rated Torque	Base Rotating Speed
618 N·m	170 kW	60 kW	218 N·m	2000 rpm

Table 7. Parameters of the motor for SHEVs

3.2.1.3. Selection of parameters for batteries

For the hybrid vehicles, the larger of battery capacity, the longer the vehicle can drive under the pure electric condition. However, larger capacity means larger weight and volume. Therefore, we should choose the battery based on several key factors, including the technical specifications of the vehicle, the specific energy and specific power of the battery. The selection of the number of batteries should be based on the needs of electric power and the mileage under pure electric condition.

First, from the aspect of the power need, the battery capacity must meet the maximum requirements of the output power of the motor. The number of batteries needed can be determined by the following formula [14]:

$$n = \frac{P_{b\max}}{(2E_b^2 / 9R_b)\eta_{mc}} \quad (18)$$

where n is the number of batteries, $P_{b\max}$ is the power needed from the battery under the worst condition (with the lowest SOC value), E_b is the electromotive force of the battery; R_b is the equivalent resistance of the battery.

As far as the mileage under pure electric condition is concerned, the number of batteries should meet the following criterion as [15]:

$$n' = \frac{P_{bc}(s / V_{bc})}{U_{\text{model}}C} \times 1000 \quad (19)$$

where, n' is the number of batteries; P_{bc} is the power under pure electric condition; s is the driving distance under pure electric condition; V_{bc} is driving speed under pure electric condition; U_{model} is the output voltage of a single battery; C is the capacity of the battery.

Finally, one can compare the values of n' and n , and the larger number should be chosen as the number of batteries.

Table 8 lists the selection results for the battery.

Capacity	Number	Rated Total Energy
93 Ah	40	44.64 kWh

Table 8. Parameters of hybrid batteries.

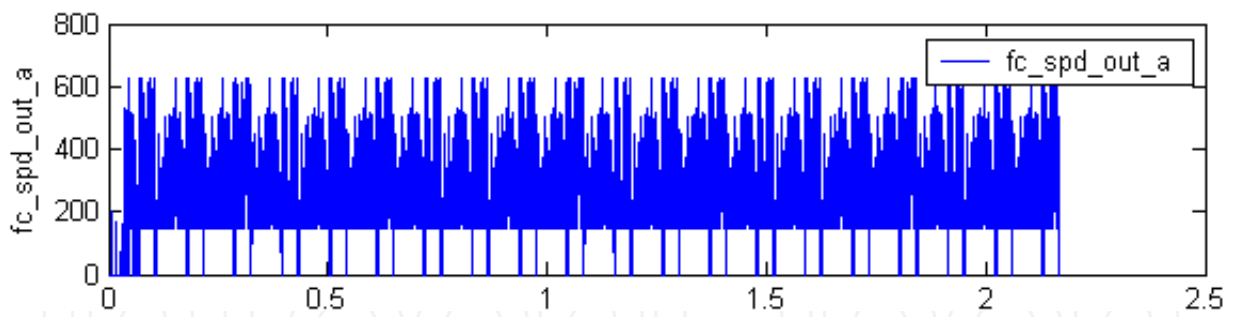


Figure 16. Output Speed of the Engine.

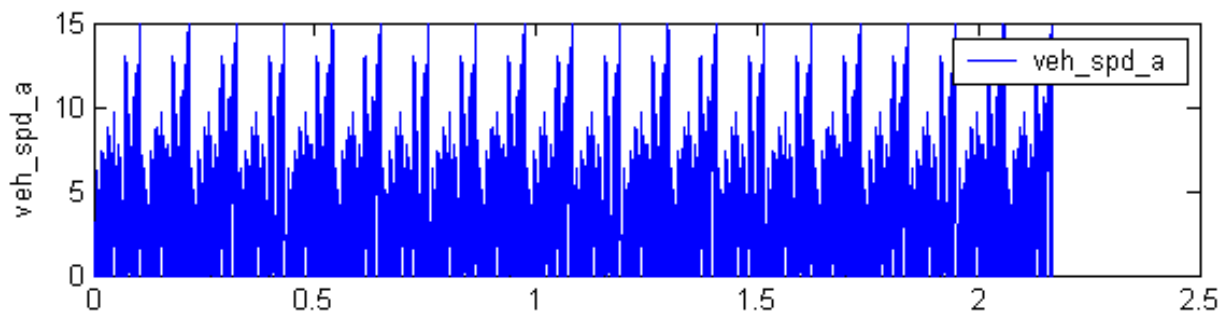


Figure 17. Vehicle Speed.

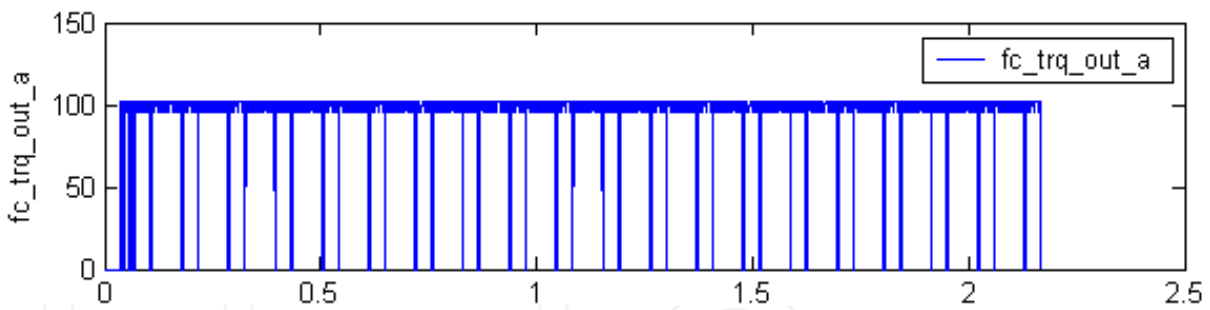


Figure 18. Output Torque of the Engine.

The simulation results indicate that through the control strategy designed in this research, the battery SOC value can be maintained at about 0.5, which completely meet the safety requirement of the battery; the average speed of the vehicle remained at the value around 40km / h, which conforms to the road and traffic conditions in most cities; from the output torque of the engine in Fig. 18 one can see that, under the control strategy designed in this research, the engine works in the best economic zone.

3.3. Summary on analysis of series hybrid electric vehicle

In this section, the simulations and analysis of the series hybrid electric vehicles (SHEVs). According to the technical specifications of SHEVs, a control strategy was designed utilizing

the power follower and thermostat, while parameters were selected for various part of the SHEV. Simulation results revealed that this control strategy can not only meet the performance requirements of the vehicle, but make the engine and batteries work in a reasonable range. The study and optimization of the control strategies are the hotspots in the field of hybrid power system. The optimization of control strategies is not only to achieve the best fuel economy, but to adjust to various operating conditions. In particular, since all the countries are implementing the environmental protection to have a greener earth, the minimum vehicle emission becomes a crucial measurement for the superiority of a control strategy for SHEVs.

4. Investigation of the temperature distribution in the Li-ion battery for pure electric vehicles

The lithium-ion batteries have much more excellent performance than the other types of batteries so that they are widely used in the electric vehicles (EVs) [16-18]. However, the Li-ion battery is very sensitive to the temperature variation. One needs to consider not only the temperature range of the batteries, but the temperature difference of each battery in the pack. Low temperature can result in insufficient electrochemical reaction inside the battery, whereas high temperature will affect the working condition so that it shortens the life of service of the battery. Furthermore, the overshoot or overdischarge may be happened in some batteries if the temperature distribution among the battery pack is nonuniform. In order to minimize the heat generated in the battery pack, the temperature distributions in the battery and the battery pack utilized in EVs are investigated and parameters are optimized to lower the temperature and non-uniformity of the temperature distribution.

4.1. FE formulations of the heat conduction equation of the li-ion battery

The heat conduction equation in the Cartesian coordinates is given as [19]:

$$\rho C \frac{dT}{dt} = \frac{\partial}{\partial x} \left(k_x \frac{\partial T}{\partial x} \right) + \frac{\partial}{\partial y} \left(k_y \frac{\partial T}{\partial y} \right) + \frac{\partial}{\partial z} \left(k_z \frac{\partial T}{\partial z} \right) + \phi_v \quad (20)$$

where ρ is the density and C is the heat capacity.

The Galerkin method is employed to obtain the finite element forms of the heat conduction equation. For the steady-state heat conduction equation, the finite element form is expressed as [20]:

$$K\phi = P \quad (21)$$

and the finite element form for the transient heat conduction equation is written as [20]:

$$K\phi + C\dot{\phi} = P \tag{22}$$

where:

$$K_{ij} = \sum_e \int_{\Omega} (k_x \frac{\partial N_i}{\partial x} \frac{\partial N_j}{\partial x} + k_y \frac{\partial N_i}{\partial y} \frac{\partial N_j}{\partial y} + k_z \frac{\partial N_i}{\partial z} \frac{\partial N_j}{\partial z}) d\Omega + \sum_e \int_{\tau_3} h N_i N_j d\tau \tag{23}$$

$$P_i = \sum_e \int_{\tau_2} N_i q d\tau + \sum_e \int_{\tau_3} h N_i \phi_a d\tau + \sum_e \int_{\Omega} N_i \rho Q d\Omega \tag{24}$$

In Eqs. (21)-(24), K is the heat conduction matrix, ϕ is the nodal temperature matrix, P is the temperature load matrix, C is the heat capacity matrix, and $\dot{\phi}$ represents the derivative of ϕ with respect to time. In addition, N_i denotes the shape function, and k_x, k_y, k_z represents the thermal conductivity along three axes.

4.2. Finite element simulations of the li-ion battery

4.2.1. Equivalent material properties of the battery

Figure 19 illustrates the rectangular Li-ion battery employed in this research. It has the height of 280 mm, the depth of 71 mm, and the width of 182 mm. The internal structure of the Li-ion battery mainly includes three parts: the shell, the contact layer and the central area. The central area is the heating zone of the battery since most reactions are occurred in the central area.



Figure 19. Internal Structure of the rectangular Li-ion battery.

The central area is the most complex area of the battery since it is stacked with hundreds of layers made of different materials. Therefore it is essentially infeasible to generate and implement finite element models of the entire battery incorporating the actual structures. Consequently, equivalent modeling techniques must be developed to investigate the temperature distribution of the battery while circumventing the time and intense computational requirements. In other words, equivalent material properties need to be calculated and utilized in the finite element models. Eqs. (25)-(28) represent the calculations of the equivalent material properties of the battery:

$$\text{Density: } \rho = \frac{m}{V} = \frac{\sum_{i=1}^n m_1 + m_2 + m_3 + \dots + m_n}{V_1 + V_2 + V_3 + \dots + V_n} \quad (25)$$

$$\text{Specific heat: } C = \frac{\sum_{i=1}^n C_1 V_1 + C_2 V_2 + C_3 V_3 + \dots + C_n V_n}{V_1 + V_2 + V_3 + \dots + V_n} \quad (26)$$

Thermal Conductivity:

$$\text{Serial Connection: } K = \frac{\sum_{i=1}^n l_i}{\sum_{i=1}^n \frac{l_i}{k_i}} \quad (27)$$

$$\text{Parallel Connection: } K = \frac{\sum_{i=1}^n A_i k_i}{\sum_{i=1}^n A_i} \quad (28)$$

where l_i denotes the length of each battery along the heat flux, whereas A_i denotes the cross-sectional area of each battery along the heat flux. Both serial and parallel connection cases have been considered and the thermal conductivity of both cases were calculated (as shown in Eq. (27)).

The material properties of the lithium-ion battery used in this research are listed in Table 9, including thickness, thermal conductivity, specific heat, density, etc.

Based on the values of the parameters provided in Table 9, the equivalent material properties of the central area in the battery can be determined:

Equivalent Density: $\rho = 2123.83 \text{ kg/m}^3$

Equivalent specific heat: $C = 1165.91 \text{ J/(kg}\times\text{K)}$

Thermal conductivity: $k_x = 1.022 \text{ W}/(\text{m}\cdot\text{K})$ $k_y = 25.746 \text{ W}/(\text{m}\cdot\text{K})$ $k_z = 26.364 \text{ W}/(\text{m}\cdot\text{K})$

	Material	Thickness	Thermal conductivity	Specific heat	Density
Anode	LiCoO ₂	0.014	1.58	1269.21	2328.5
Anode current collector	AL	0.002	238	903	2702
Negative electrode	Graphite	0.0116	1.04	1437.4	1347.33
Negative collector	Cu	0.0014	398	385	8933
Diaphragm	Polyethylene	0.0035	0.3344	1978.16	1008.98
Contact layer	Electrolyte	0.05	0.6	2055.1	1129.95
Shell	AL	0.07	238	903	2702

Table 9. Material properties of the Lithium-ion battery.

4.2.2. Discussion of boundary conditions

The Li-ion battery used in this research has a rectangular shape, which means it is under the natural convection if there is no dissipation source. Under the natural convection, the heat transfer is mainly generated by the buoyancy of the air, so different boundary surfaces may have different convection coefficients. The convection coefficient for each boundary surface needs to be calculated separately. In this study, the constant temperature of the wall is set to be 30 °C, the thermal conductivity is set as $k = 2.63 \times 10^{-2} \text{ W}/(\text{m}\cdot\text{k})$, the kinematic viscosity is $\nu = 15.53 \times 10^{-6} \text{ m}^2/\text{s}$, and the Prandtl number is $\text{Pr} = 0.702$.

For the top surface of the battery, the heat can be easily dissipated so that the heat convection is strong. The calculations of the convection coefficient can be shown as follows:

$$\text{Grashof number: } Gr = \frac{g\alpha\Delta t l^3}{\nu^2} = 2.26 \times 10^4$$

$$\Rightarrow \text{Raleigh number: } Ra = Gr \times \text{Pr} = 1.5865 \times 10^4$$

$$\Rightarrow \text{Nusselt number: } Nu = 0.54 Ra^{\frac{1}{4}} = 6.06$$

$$\Rightarrow \text{Convection coefficient: } h = Nu \frac{k}{l} = 6.25 \text{ W}/(\text{m}^2 \cdot \text{K})$$

For the bottom surface of the battery, the heat convection is weak.

$$Nu = 0.27 Ra^{\frac{1}{4}} = 3.03 \Rightarrow h = Nu \frac{k}{l} = 3.125 \text{ W}/(\text{m}^2 \cdot \text{K})$$

For the vertical surfaces, they should have the same convection coefficients:

$$Gr = 2.9772296 \times 10^7 \quad Nu = 39.89 \quad h = Nu \frac{k}{l} = 3.75 \text{ W}/(\text{m}^2 \cdot \text{K})$$

4.2.3. Finite element simulations

There are two types of most commonly used Li-ion batteries, one with a cylindrical shape and the other with a rectangular shape. Figure 20 illustrates the temperature distributions in these two different types of Li-ion batteries.

It can be seen that under the same condition (1C electric charge and at the temperature of 293K), the maximum temperature in the cylindrical battery is 326.12K and the largest temperature difference in the battery is 8.57K; while the maximum temperature in the rectangular battery is 320.58K and the largest temperature difference in the battery is 6.33K. It indicates that the rectangular battery is better than the cylindrical one in terms of heat dissipation.

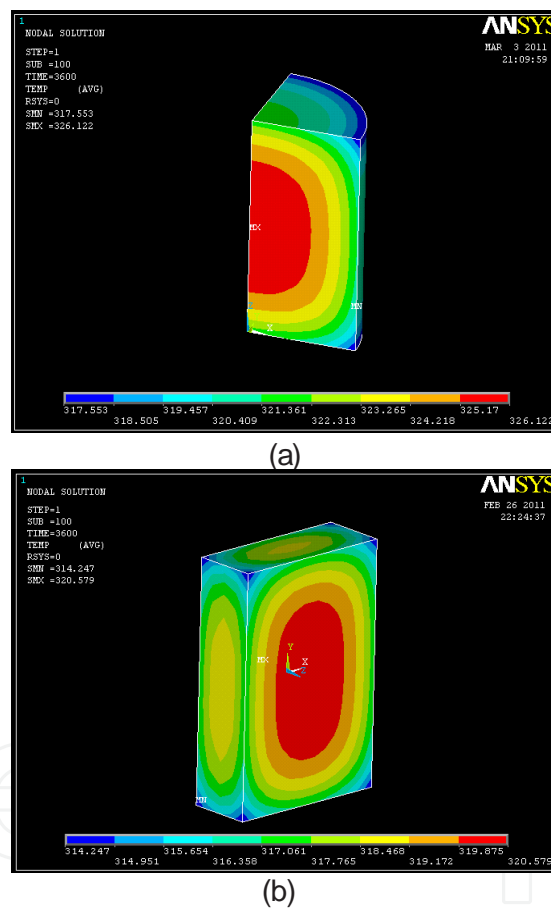


Figure 20. Temperature Distribution of (a) cylindrical battery and (b) rectangular battery at 1C293K.

The effect of the discharge rate of the battery on the temperature distribution of the battery pack was also investigated. Figure 21 illustrates the temperature distribution in the battery with different discharge rates. The comparison between Fig. 21(a) and Fig. 21(b) reveals that the temperature of the battery with a faster discharge rate is higher than the temperature of the battery with a slower discharge rate. A slower discharge rate should be chosen to lower the temperature and decrease the temperature difference in the battery. Due to the demand

of high power, EVs usually employ battery packs in which each pack consists of tens of batteries. Figure 22 shows a typical Li-ion battery pack used in the EVs [21].

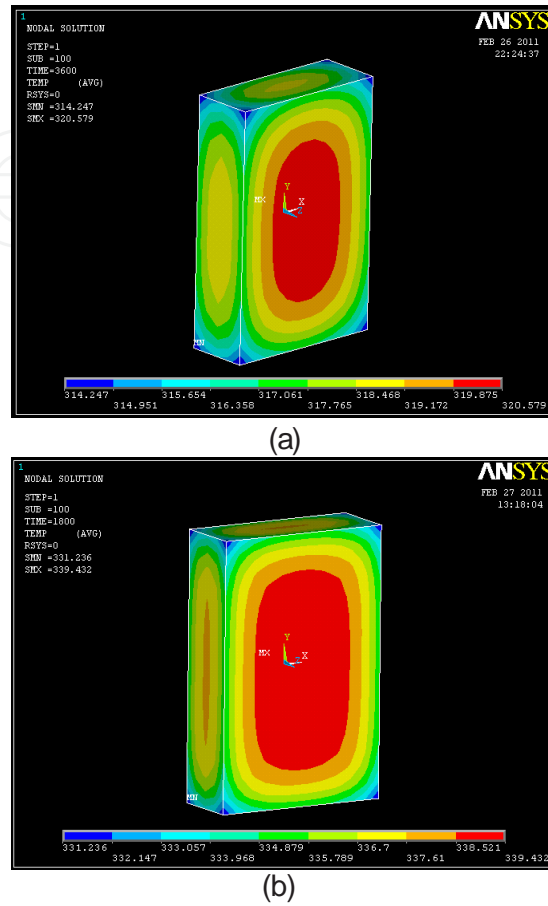


Figure 21. Temperature distribution in the battery at (a) 1C discharge and (b) 2C discharge.



Figure 22. A typical Li-ion battery pack utilized in the EVs [21].

The cooling strategy of the battery pack is investigated by considering two different strategies. In the first strategy, the cooling gas (air) is blowing along the longitudinal direction of the battery pack, it is called the serial cooling; in the second strategy, the cooling direction is perpendicular to the longitudinal direction of the pack, it is called the parallel cooling.

Figure 23 illustrates the temperature distributions in the battery pack using the serial cooling strategy with two wind speeds (4 m/s and 10 m/s). The choice of these two values is based on the critical wind speed (4.2 m/s), calculated based on the critical Reynolds number of 500000 to differentiate the laminar flow and the turbulent flow.

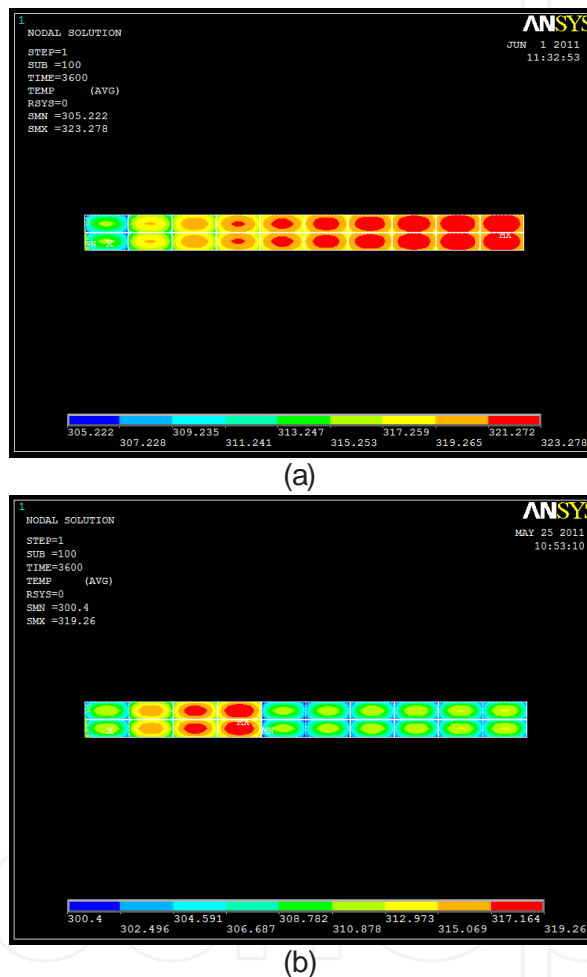


Figure 23. Temp. Distributions in the battery pack with the wind speed of (a) 4 m/s and (b) 10 m/s.

It can be seen in Fig. 23(a) that the air flow will turn to be the turbulent flow at the speed of 10 m/s which is much larger than the critical value of the wind speed (4.2 m/s). Furthermore, it can be seen that there are quite large temperature differences (about 19 degrees) in the battery pack for both wind speeds, which will deteriorate the batteries in the long term.

The temperature distributions in the battery pack using the parallel cooling strategy is presented in Fig. 24. The battery pack is under the condition of 1C electric charge and 293K

temperature. The convection coefficient is $50 \text{ W/m}^2 \text{ K}$. It can be seen that the maximum temperature difference in the battery pack is less than 7 degrees. The temperature distribution is the same for each battery. Comparing Figs. 23 and 24, one can easily see that the parallel cooling strategy is much better than the serial cooling strategy in this category.

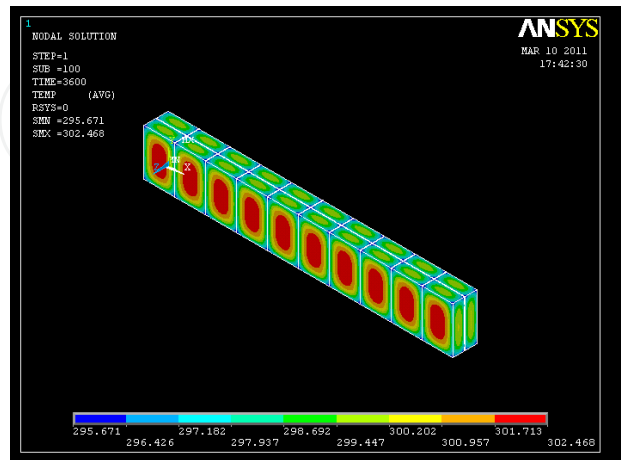


Figure 24. Temperature distribution in the battery pack utilizing the parallel cooling.

4.3. Summary on investigation of the temperature distribution in the Li-ion battery

In this section, the finite element formulations of the heat conduction equation of the Lithium-ion battery are established for both steady state and transient state cases. Then the boundary conditions of the battery were discussed and the heat convection coefficients were determined for each surface of the battery. A parametric study was developed to investigate and optimize the temperature distribution in the battery. Finite element results indicate that a rectangular shape battery should be chosen to minimize the temperature difference in the battery. Results also revealed that a slower discharge rate needs to be selected to not only lower the temperature inside the battery, but make the temperature distribution in the battery as uniform as possible. Finally, the Li-ion battery pack was investigated and different cooling strategies were studied. Investigation indicates that the parallel cooling should be chosen to accelerate the heat dissipation and minimize the temperature difference in the battery pack. To acquire more accurate results on the temperature distribution in each battery and the entire battery pack, much more sophisticated finite element models need to be established to simulate the real structure inside the battery.

5. Summary and conclusions

In this chapter, the mechanical behaviors of the electric vehicles were investigated to improve the performance of the electric vehicles such that they can prevail over the conventional petroleum vehicles in the near future. Three different aspects of the electric vehicles were analyzed and substantially improved via the use of various methods.

Firstly, the regenerative braking force in the pure electric vehicle was analyzed and the distribution range of the braking forces in the front and rear wheels was determined to meet the requirements in UNECE R13. An optimized control strategy of the regenerative braking process was proposed based on the results of the analysis. Simulation results indicate that this optimized control strategy can considerably improve the energy efficiency of the regenerative braking process, as well as that of the entire vehicle. This optimized control strategy can also be used for hybrid vehicles.

Secondly, series-hybrid electric vehicles (SHEVs) were investigated to improve the efficiency of the engine and the working condition of the battery. According to the technical specifications of SHEVs, a control strategy was designed utilizing the power follower and thermostat, while parameters were selected for various part of the SHEV. Simulation results revealed that this control strategy can not only meet the performance requirements of the vehicle, but make the engine and batteries work in a reasonable range. The study and optimization of the control strategies are the hotspots in the field of the hybrid power system.

Finally, the temperature distribution in the lithium-ion battery for pure electric vehicles are studied and analyzed. Finite element formulations of the heat conduction equation of the Lithium-ion battery; boundary conditions of the battery were discussed and the heat convection coefficients were determined for each surface of the battery; then a parametric study was developed to investigate and optimize the temperature distribution in the battery. Results indicate that a rectangular shape battery should be chosen to minimize the temperature difference in the battery and a slower discharge rate is needed to make the temperature distribution in the battery as uniform as possible.

The research and study developed in this chapter have not only substantial theoretical values but also significant practical values. The results obtained in this chapter provide clear guidelines for the electric vehicle manufacturers to improve the quality and competitiveness of the electric vehicles such that they will be able to prevail the automobile industry in the near future.

Author details

Liang Zheng

Address all correspondence to: liangzheng@hitsz.edu.cn

Harbin Institute of Technology Shenzhen Graduate School, University Town of Shenzhen, Shenzhen, China

References

- [1] Kawashima K., Uchida T., and Hori Y. Rolling stability control of in-wheel electric vehicle based on two-degree-of-freedom control. International Workshop on Advanced Motion Control, AMC, 2008 (1): 751-756.

- [2] Weissinger C., Buecherl D., and Herzog H.-G. Conceptual design of a pure electric vehicle. IEEE Vehicle Power and Propulsion Conference, 2010.
- [3] Wang R.-R., Chen Y., Feng D.-W., Huang X.-Y., and Wang J.-M. Development and performance characterization of an electric ground vehicle with independently actuated in-wheel motors, *Journal of Power Sources*, 2011, 196(8): 3962-3971.
- [4] Younis A., Zhou L., and Dong Z.-M. Application of the new SEUMRE global optimization tool in high efficiency EV/PHEV/EREV electric mode operations, *International Journal of Electric and Hybrid Vehicles*, 2011, 3(2): 176-190.
- [5] http://en.wikipedia.org/wiki/Regenerative_brake
- [6] Official website of United Nations Economic Commission for Europe <http://www.unece.org/trans/main/wp29/wp29regs1-20.html>
- [7] http://en.wikipedia.org/wiki/Hybrid_vehicle#Series_hybrid
- [8] Xiong J., Wang G. Hybrid electric bus development and industrialization. *Bus Technology and Research (in Chinese)*, 2002, 3: 4-6.
- [9] Li X.-Y., Yu X.-M., and Wu Z.-X. Series Hybrid Electric Vehicle Control Strategy. *Journal of Jilin University: Engineering Science*, 2004, 35: 250-254.
- [10] Wipke K. B., Cuddy M. R. and Burch S. B. ADVISOR 2.1: A User Friendly Advanced Powertrain Simulation Using a Combined Backward / Forward Approach. NREL/JA-540-26839, 1999.
- [11] Wang P. and Sun J. Design and Simulation of Series Hybrid Transit Bus". *Journal of Technology and Research (in Chinese)*, 2007(11): 42-43.
- [12] Yu Z.-S., editor, *Automotive theory*. Mechanical Industry Press, 2003.
- [13] Zhu S.-S., Zhu W.-D. Study on the matching of generator and Motor in Series Hybrid Electric Bus. *Journal of R & D of Automobiles (in Chinese)*, 2001(6): 46-48.
- [14] Yang X., Qian L.-J. Series Hybrid Electric Bus parameter selection and simulation. *Bus Technology (in Chinese)*, 2006(1): 25-27.
- [15] Khanipour A., Ebrahimi K., and Seale W. J. Conventional Design and Simulation of an Urban Hybrid Bus, *Engineering and Technology*. 2007(28): 26-32.
- [16] Einhorn M., Roessler W.; and Fleig J. Improved performance of serially connected Li-ion batteries with active cell balancing in electric vehicles. *IEEE Transactions on Vehicular Technology*, 2011, 60(6): 2448-2457.
- [17] Bandhauer T. M., Garimella S., and Fuller T. F. A critical review of thermal issues in lithium-ion batteries. *Journal of the Electrochemical Society*, 2011, 158(3), R1-R25.
- [18] Guerrero C. P., Li J.-S., Biller S., and Xiao G.-X.: Hybrid/electric vehicle battery manufacturing: The state-of-the-art, 2010 IEEE International Conference on Automation Science and Engineering, 2010, 281-286.

- [19] Holman J. P. Heat Transfer, ninth edition, p. 4, McGraw-Hill (2002).
- [20] Cook R. D., Malkus D. S., Plesha M. E. and Witt R. J. Concepts and Applications of Finite Element Analysis, fourth edition, p. 464-466, John Wiley (2001).
- [21] <http://en.wikipedia.org/wiki/File:Lithium-Ionen-Accumulator.jpg>.

IntechOpen

IntechOpen

